Acta Pharmaceutica Sinica B 2026;16(7):4575−4591

Chinese Pharmaceutical Association
Institute of Materia Medica, Chinese Academy of Medical Sciences

Acta Pharmaceutica Sinica B

www.elsevier.com/locate/apsb
www.sciencedirect.com

ORIGINAL ARTICLE

Targeting bacterial phosphotransferase system to prevent the dissemination of antibiotic resistance genes

Miao Zhang[a], Bingqing Yang[a], Jingyi Sun[a], Zhiqiang Wang[a,b,c], Yuan Liu[a,b,c,*]

[a]*Jiangsu Co-innovation Center for Prevention and Control of Important Animal Infectious Diseases and Zoonoses, College of Veterinary Medicine, Yangzhou University, Yangzhou 225009, China*
[b]*Joint International Research Laboratory of Agriculture and Agri-Product Safety, the Ministry of Education of China, Yangzhou University, Yangzhou 225009, China*
[c]*Institute of Comparative Medicine, Yangzhou University, Yangzhou 225009, China*

Received 14 July 2025; received in revised form 26 March 2026; accepted 16 April 2026

KEYWORDS

Antimicrobial resistance;
Plasmid;
Horizontal gene transfer;
Inhibitor;
Indole analogs;
Phosphotransferase system;
Enolase;
Energy supply

Abstract Antimicrobial resistance (AMR) poses a significant challenge to public health and human security, with plasmid-mediated horizontal gene transfer (HGT) being a primary driver for its dissemination. Here, we identify indole analogs containing electron-withdrawing groups as a new category of HGT inhibitors. Using indole-3-acetic acid (IAA) as a representative scaffold, we demonstrate that IAA targets glycolytic enolase to deplete phosphoenolpyruvate (PEP) in donor bacteria; this suppresses phosphotransferase system (PTS) activity, blocks PtsI phosphorylation, reduces cAMP synthesis and prevents catabolite repressor protein (CRP) activation, ultimately limiting intracellular ATP availability. Concurrently, IAA attenuates reactive oxygen species (ROS) generation by inhibiting $FADH_2$ oxidation and riboflavin biosynthesis. The concerted reduction in ATP and ROS arrests conjugative plasmid transfer. Overall, our work suggests the potential of indole analogs as a new class of conjugative transfer inhibitors and highlights that bacterial phosphotransferase system represents a promising target to prevent the propagation of AMR.

*Corresponding author.
E-mail address: liuyuan2018@yzu.edu.cn (Yuan Liu).

Peer review under the responsibility of Chinese Pharmaceutical Association and Institute of Materia Medica, Chinese Academy of Medical Sciences.

https://doi.org/10.1016/j.apsb.2026.04.021

1. Introduction

The clinical deployment of antibiotics has imposed unprecedented selective pressure on bacterial populations, accelerating the evolution and dissemination of antimicrobial resistance (AMR)[1]. Mobile genetic elements, particularly conjugative plasmids, drive rapid adaptation by facilitating horizontal gene transfer (HGT) of resistance determinants across species boundaries[2,3]. Critical Gram-negative pathogens[4], including *Escherichia coli*, *Salmonella enterica* and *Klebsiella pneumoniae*, have acquired multidrug-resistant (MDR) phenotypes through plasmid-mediated antibiotic resistance genes (ARGs), such as bla_{NDM} (carbapenem resistance gene)[5], *mcr-1* (colistin resistance gene)[6], and *tet*(X3/X4) (tigecycline resistance gene)[7], threatening the efficacy of last-resort therapeutic agents.

Inhibition of conjugative transfer represents a chemoprophylactic strategy to curtail resistance spread without imposing bactericidal selection. Diverse inhibitor classes have been identified, including fatty acids[8,9], polysaccharide antibiotics[10], small molecules[11] and nanomaterials[12]. Mechanistically, these compounds typically exert their inhibitory effects primarily by targeting the key processes involved in plasmid transfer. Specific examples include disrupting bacterial T4SS[13], impairing bacterial energy metabolism[14], as well as suppressing the generation of reactive oxygen species (ROS) and the activation of SOS responses[15]. Structure−activity relationship studies have elucidated specific pharmacophore requirements. For instance, 2-alkynoic fatty acids require a terminal carboxylic group, an optimal 16-carbon aliphatic chain and defined unsaturation patterns for maximal inhibitory potency[16]. Similarly, synthetic small molecules, including C10 and KSK85, exert their effects by interfering with T4SS-dependent assembly processes[13]. Additionally, approved therapeutics such as azidothymidine (an anti-HIV drug) have shown broad-spectrum HGT inhibition by dissipating proton motive force, thereby depleting intracellular ATP reserves and attenuating flagellar motility[17]. Despite these efforts, no HGT inhibitors targeting bacterial phosphotransferase systems (PTS) have been reported to date. Moreover, no HGT inhibitors have achieved clinical approval, underscoring the urgent need for novel pharmacophores with distinct modes of action.

Indoles and their derivatives are heterocyclic biologically active molecules, ubiquitous in amino acid metabolites (tryptophan), neurohormones (melatonin) and phytohormones[18]. Beyond their diverse pharmacological activities (antimicrobial, anti-inflammatory, antitumor)[19], indoles function as intercellular signaling molecules modulating bacterial physiology, including plasmid stability[20], biofilm formation[21,22], and virulence[23]. Notably, our previous study also showed that indoles and their derivatives contribute to enhancing the antibacterial activity of bactericidal agents against tolerant or persister cells[24]. Indoles and their derivatives, as natural products, possess the advantages of natural sources, easy availability and low toxicity[23], and represent potential HGT inhibitor candidates. For example, our previous study has demonstrated that melatonin, a methoxyindolamine compound, inhibits the conjugative transfer of plasmid-borne ARGs in *Escherichia coli* by disrupting bacterial proton motive force[25]. Xiong et al.[26] identified that indole inhibits the IncP-1 conjugation system primarily by upregulating the expression of *korA* and *korB*. Nevertheless, systematic exploration of structure−activity relationships within the indole pharmacophore, and identification of specific metabolic targets mediating conjugation inhibition, remain elusive.

In this study, we discovered that indole analogs carrying electron-withdrawing groups are a promising category of HGT inhibitors. Mechanistically, IAA inhibited enolase activity and interfered with PtsI phosphorylation, thereby reducing cAMP synthesis and diminishing intracellular ATP levels. Meanwhile, IAA reduced ROS accumulation by inhibiting $FADH_2$ oxidation and diminishing riboflavin synthesis. Collectively, our findings reveal the potential of indole analogs as a new class of HGT inhibitors to block the dissemination of AMR.

2. Results

2.1. Indole analogs inhibit conjugative plasmid transfer

To evaluate the potential of indole-based compounds in controlling antibiotic resistance dissemination and to elucidate their structure−activity relationships (SAR), we screened 12 indole analogues for inhibition of RP4-7 plasmid conjugative transfer between *E. coli* DH5α (donor) and *E. coli* EC600 (recipient). Bacterial conjugation requires direct cell-to-cell contact for plasmid transfer *via* the type IV secretion system (T4SS). Following co-incubation, transconjugants were selected using plasmid-encoded antibiotic resistance markers, and transfer frequencies were quantified (Fig. 1A).

We first determined the minimum inhibitory concentrations (MICs) of these compounds against both strains to establish non-inhibitory concentrations for conjugation assays. Most compounds exhibited MICs of 125 μg/mL against both strains, with the exception of 5-iodo-1*H*-indole (MIC = 62.5 μg/mL; Supporting Information Table S1). Notably, 5-methylindole and 5-hydroxyindole-3-acetic acid failed to inhibit conjugation, whereas the remaining ten compounds significantly suppressed plasmid transfer (Fig. 1B and Supporting Information Fig. S1). Growth curve analyses and colony count confirmed that 10 μg/mL of these derivatives did not affect bacterial viability (Supporting Information Figs. S2 and S3).

To dissect the SAR, we categorized these compounds based on their side-chain functionalities: four haloindoles, five carboxylic acid-bearing indoles, and three substituted with $-NO_2$, $-CHO$ and $-CH_3$ groups, respectively (Fig. 1C). Indole comprises a pyrrole ring fused to a benzene ring, with substitutable positions at C3, C5 and C7. Structure−activity analysis revealed that electron-withdrawing groups (EWGs) at these positions correlated with inhibitory potency (Fig. 1D). For instance, 5-methylindole, bearing the electron-donating $-CH_3$ group, failed to inhibit plasmid transfer, whereas compounds with strong EWGs showed potent activity.

We further quantified these electronic effects using quantitative structure−activity relationship (QSAR) modeling. For seven compounds with direct ring substituents, Hammett σ constants correlated strongly with conjugative transfer frequencies (Fig. 1E), indicating that electron-withdrawing capacity on the indole ring drives inhibitory activity. Conversely, for five compounds with aliphatic side chains (indole-3-carboxylic acid to indole-3-butyric acid), Taft σ^* values showed no significant correlation (Fig. 1F), demonstrating that side-chain length effects are not governed by inductive electronic effects.

We next validated these findings using clinical isolates harboring resistance plasmids, including bla_{NDM-5}-positive *K. pneumoniae* C12 and *E. coli* L65; *tet*(X4)-positive *E. coli* RS3-1

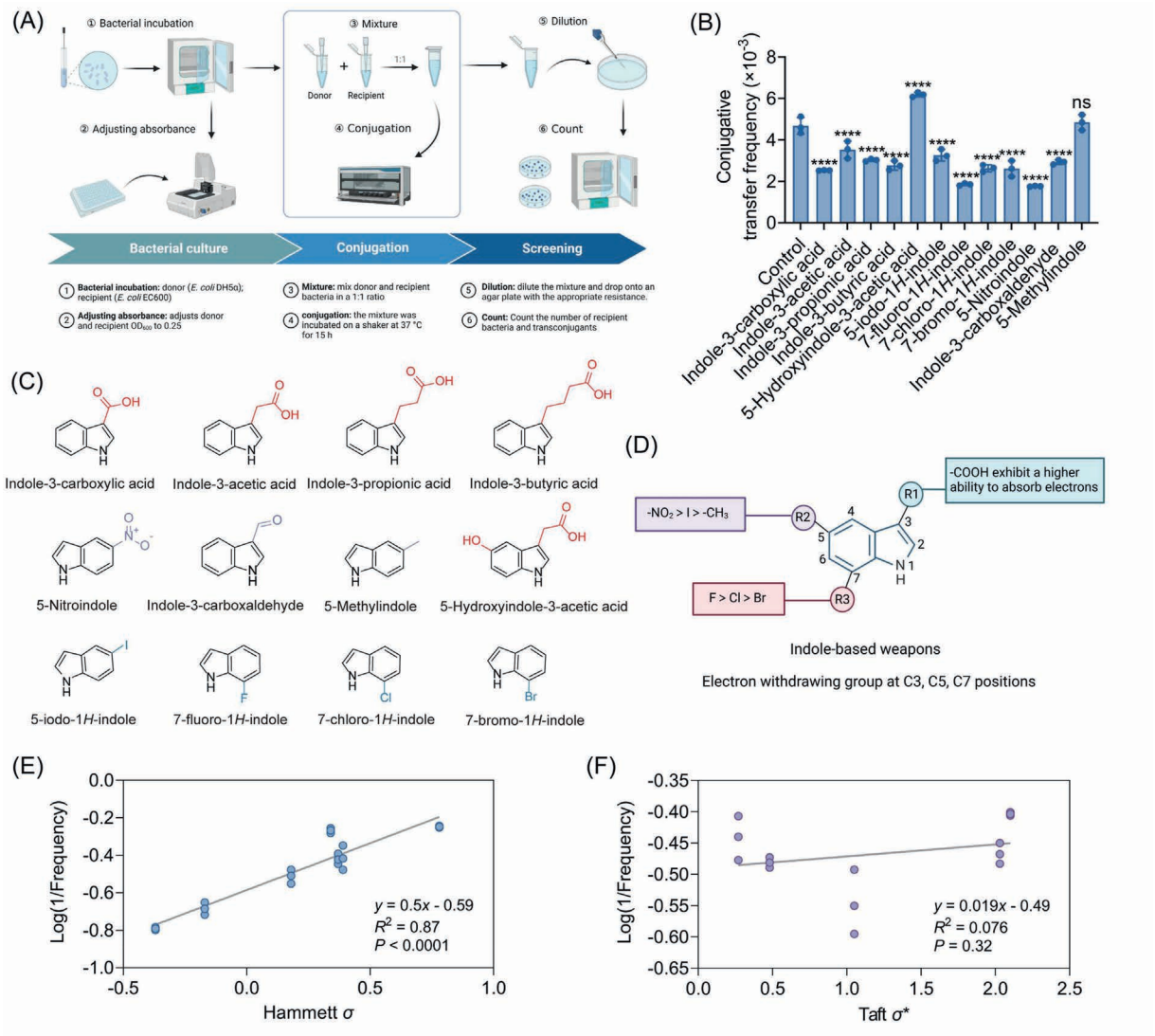

Figure 1 Structure−activity relationship of indole analogues as conjugation inhibitors. (A) Schematic diagram of assays for the determination of conjugative transfer frequency. (B) Conjugative transfer frequency of RP4-7 plasmid from the donor bacteria (*E. coli* DH5α) to the recipient bacteria (*E. coli* EC600) in the presence of 12 indole derivatives. (C) Chemical structures of 12 indole derivatives. The distinct categories of side-chain groups are indicated in red, blue and purple, respectively. (D) Electron-withdrawing capacity of side-chain groups of indole derivatives at C3, C5 and C7 positions. (E) Linear correlation between Hammett substituent constants (σ) of indole ring substitutions and the conjugative transfer frequency. The *y*-axis shows $\log_{10}$(1/conjugative transfer frequency). (F) Correlation analysis between Taft polar substituent constants (σ*) of the side-chain modifications and the conjugative transfer frequency. The *y*-axis shows $\log_{10}$(1/conjugative transfer frequency). Data are presented as mean ± SD ($n = 3$). Statistical significance was determined by unpaired Student's *t*-test ($^{****}P < 0.0001$; ns, not significant).

and RF2-1; and *mcr-1*-positive *E. coli* LD67-1. In line with the results obtained using engineered strains, three compounds were found to significantly suppress the conjugative transfer of three clinically relevant plasmids (Fig. 2). This inhibitory effect was not limited to a specific genus but was observed across strains of various genera, ranging from *K. pneumoniae* to *E. coli* (Fig. 2C). Notably, these compounds exhibited a biphasic effect on *mcr-1*-positive plasmids, promoting transfer at low concentrations while inhibiting at high concentrations (Fig. 2A). Given its potent inhibitory activity, natural occurrence as a gut microbiota tryptophan metabolite[27] and established biosafety profile[28], IAA was selected for subsequent mechanistic investigations.

2.2. *IAA reprograms bacterial metabolism to restrict energy supply*

To elucidate the mechanism underlying IAA-mediated inhibition of horizontal gene transfer, we investigated its impact on bacterial metabolism. Plasmid conjugation is an energy-intensive process dependent on ATP availability[29]; therefore, we performed untargeted metabolomics on donor (*E. coli* DH5α) and recipient (*E. coli* EC600) bacteria following IAA treatment (10 μg/mL). Partial least squares discriminant analysis (PLS-DA) of donor metabolomes revealed clear separation between control and IAA-treated groups (Fig. 3A). Of 1063 quantified metabolites, 203 exhibited

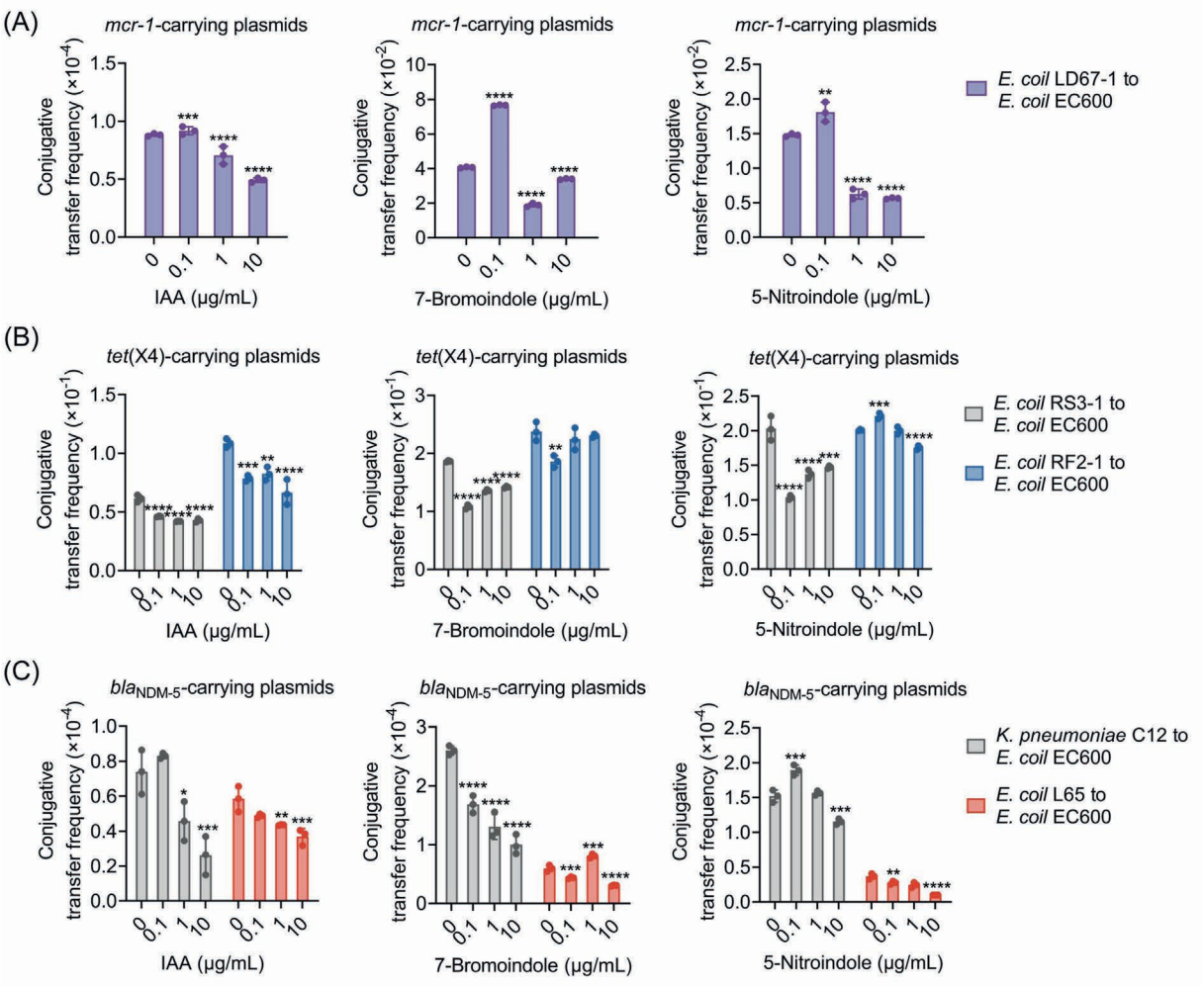

Figure 2 Indole derivatives inhibit conjugative transfer of clinical resistance plasmids. (A) Effect of IAA, 7-bromoindole and 5-nitroindole on conjugative transfer of *mcr-1*-carrying plasmids. (B) Conjugative transfer frequency of *tet*(X4)-carrying plasmids under indole treatments. (C) Frequency of conjugative transfer of $bla_{\text{NDM-5}}$-carrying plasmids upon exposure to IAA, 7-bromoindole and 5-nitroindole. Data are presented as mean ± SD ($n = 3$). Statistical significance was determined by one-way ANOVA ($^{*}P < 0.05$, $^{**}P < 0.01$, $^{***}P < 0.001$, $^{****}P < 0.0001$).

significant differential abundance ($P < 0.05$), with 126 upregulated and 77 downregulated following IAA exposure (Fig. 3B). Hierarchical clustering and variable importance in projection (VIP) analysis identified phosphoenolpyruvate (PEP), agmatine, uric acid and 4-guanidinobutanoic acid as significantly depleted, whereas L-glutamine, deoxyinosine and trehalose accumulated (Fig. 3C and D). KEGG pathway analysis indicated profound disruption of energy metabolism and cofactor biosynthesis (Fig. 3E and F). Recipient bacteria displayed analogous metabolic alterations, with energy metabolism similarly affected (Supporting Information Fig. S4), suggesting IAA induces convergent metabolic reprogramming in both mating partners.

We next validated these metabolic alterations functionally. Resazurin-based respiration assays demonstrated significantly reduced respiration levels in both donor and recipient bacteria following IAA treatment (Fig. 3G and H). Concordantly, intracellular ATP concentrations and expression of ATP synthesis-related genes (*atpA/B/C/D*) markedly decreased in both strains (Fig. 3I and J). To establish causality between ATP limitation and conjugation inhibition, we genetically manipulated cellular energy status. Deletion of *mdh* (malate dehydrogenase), a critical TCA cycle enzyme, reduced intracellular ATP levels and consequently diminished conjugative transfer frequency of RP4-7 plasmids, whereas deletion of *cydB* (cytochrome bd oxidase) increased ATP availability and enhanced transfer (Supporting Information Fig. S5). Furthermore, supplementation with nutrient-rich medium restored ATP levels and rescued conjugation efficiency in IAA-treated cultures (Fig. 3K), confirming that metabolic restriction mechanistically underlies the inhibitory effect.

Finally, we examined whether energy depletion affects the conjugative machinery itself. RT-qPCR analysis revealed that IAA treatment downregulated expression of T4SS-encoding genes (Fig. 3L), which require ATP to drive apparatus assembly and plasmid translocation[30]. Collectively, these results demonstrate that IAA suppresses resistance plasmid transfer by reprogramming bacterial metabolism, thereby depleting intracellular ATP reserves and compromising the energetic capacity required for T4SS function.

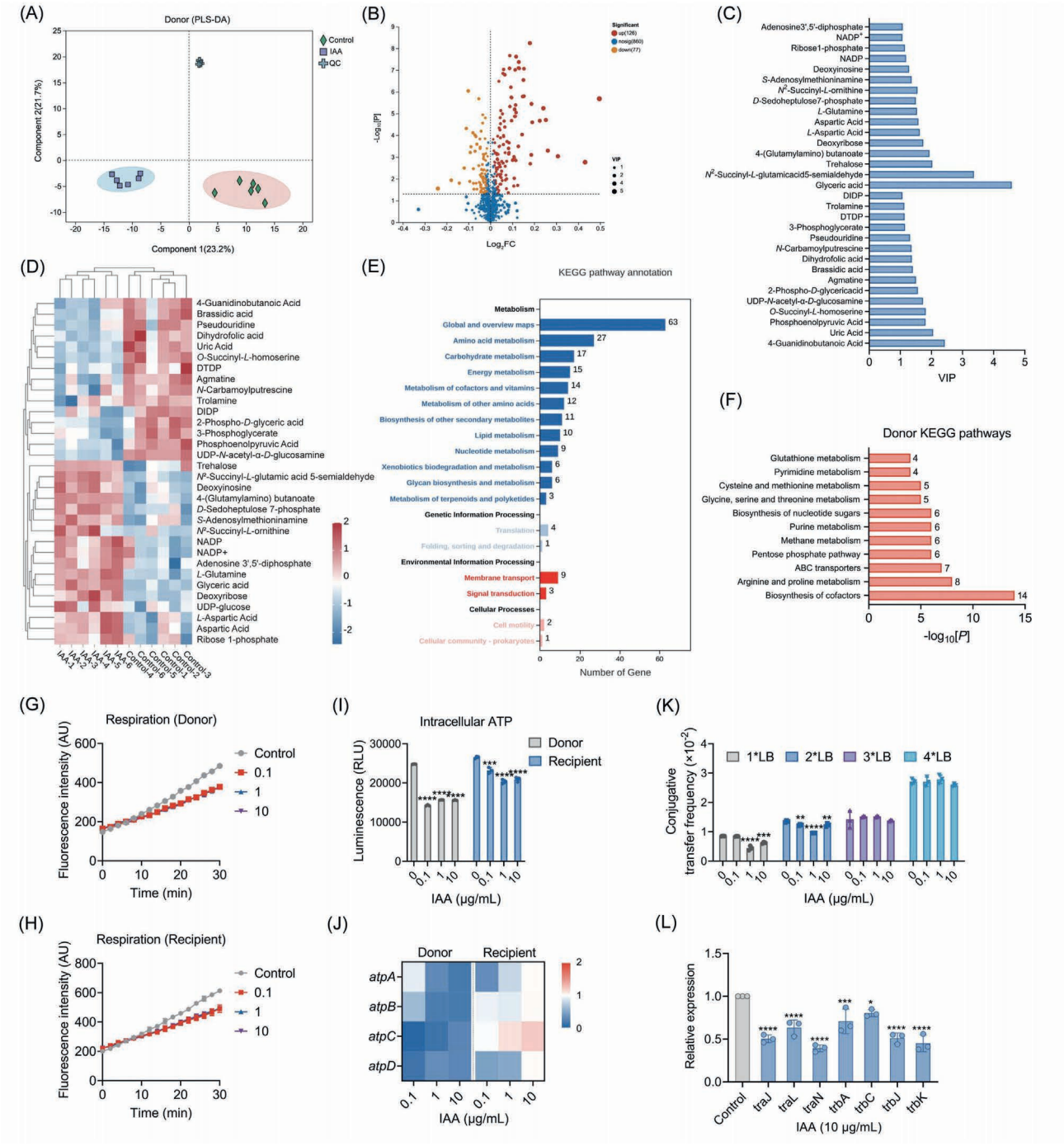

Figure 3 IAA disrupts bacterial energy metabolism and depletes ATP. (A) PLS-DA analysis of metabolites between control and IAA groups. (B) Volcano plot displaying the number of up- and down-regulated metabolites after IAA treatment in the donor bacteria. (C) Plot of VIP scores for differentially expressed metabolites (DEMs). The higher the VIP score, the stronger the contribution of the metabolite to the discriminatory characterization between the sample groups. (D) The heatmap presents the DEMs abundance in the control and IAA groups, ranging from blue to red to represent abundance from low to high. (E and F) KEGG metabolic pathway annotation of DEMs. (G and H) Respiration levels of donor (G) and recipient bacteria (H) after exposure to varying concentrations of IAA, monitored using the fluorescent probe resazurin (0.1 μg/mL). (I) Intracellular ATP levels in the donor and recipient bacteria treated with IAA. (J) mRNA expression levels of genes involved in ATP synthesis. (K) The conjugative transfer frequency of RP4-7 plasmid when incubation medium is 1 × LB, 2 × LB, 3 × LB, 4 × LB. (L) mRNA expression levels of T4SS-associated genes in response to IAA treatment. Data are presented as mean ± SD ($n = 3$). Statistical significance was determined by one-way ANOVA ($^{*}P < 0.05$, $^{**}P < 0.01$, $^{***}P < 0.001$, $^{****}P < 0.0001$).

2.3. IAA targets the phosphotransferase system to block conjugation

To identify the metabolic effectors mediating IAA-dependent inhibition, we screened eight metabolites significantly depleted by IAA treatment for their ability to rescue conjugation (Supporting Information Fig. S6). Among these, phosphoenolpyruvate (PEP), agmatine, trolamine and uric acid restored conjugative transfer frequencies when supplemented to IAA-treated cultures (Fig. 4A and Supporting Information Fig. S7). Given that PEP serves as both a glycolytic intermediate and the obligate phosphoryl donor for the phosphotransferase system (PTS)[31], we focused subsequent mechanistic studies on this metabolite.

Notably, the results showed that exogenous PEP supplementation reversed IAA-mediated suppression of both conjugative transfer and intracellular ATP levels in a dose-dependent manner (Fig. 4B and C). Concordantly, IAA treatment significantly reduced intracellular PEP concentrations in donor bacteria (Fig. 4D). Since PEP donates its phosphoryl group to enzyme I (EI, encoded by *ptsI*) to initiate the PTS phosphorylation cascade (EI, HPr, EIIA, EIIBC, carbohydrate) (Fig. 4E)[32,33], we assessed PTS activity directly. The results indicated that IAA exposure dose-dependently inhibited PTS activity (Fig. 4F).

To dissect which PTS components[34] are essential for conjugation, we generated knockout strains lacking *ptsI* (EI), *ptsH* (HPr), *crr* (EIIA), *ptsG* (EIIBC) or *ptsHI* (promoter). Interestingly, the results showed that disruption of the phosphoryl relay components (*ptsI*, *ptsH*, *crr*), but not the carbohydrate transporter *ptsG*, reduced intracellular ATP and conjugative transfer frequencies (Fig. 4G and H), indicating that early phosphorelay activity rather than late-stage PTS carbohydrate transport is required for plasmid transfer.

Afterward, we attempted to explore how IAA affects PTS activity. As the PTS acts primarily through a phosphorylation cascade reaction[35], we hypothesized that IAA inhibits PTS by dephosphorylating EI. Western blot analysis revealed that IAA treatment specifically reduced EI phosphorylation without affecting EIIA phosphorylation status (Fig. 4I and J). To validate the functional significance of this modification, we engineered two phosphorylation-deficient mutants, including *ptsI* H189Q (Δ*ptsI*/pBAD44*ptsI*-p) and *crr* H91Q (Δ*crr*/pBAD44*crr*-p)[36,37]. Both mutations phenocopied IAA treatment, reducing intracellular ATP and conjugation frequency (Fig. 4K−N). Conversely, complementation and overexpression of *ptsI* (Δ*ptsI*/pBAD44*ptsI* and MG1655/pBAD44*ptsI*) or *crr* (Δ*crr*/pBAD44*crr* and MG1655/pBAD44*crr*) increased ATP levels and conjugation, confirming that PTS phosphorelay activity is rate-limiting for plasmid transfer.

EI phosphorylation drives adenylate cyclase to synthesize cyclic AMP (cAMP), which activates catabolite repressor protein (CRP) to regulate ATP synthesis[38] and *traJ* expression in F-type plasmids[39,40]. Consistently, we found that IAA treatment and *ptsI* mutations (knockout and H189Q) both reduced intracellular cAMP levels (Fig. 5A). Furthermore, *crp* deletion recapitulated the ATP-depletion and conjugation-deficient phenotype (Fig. 5C and D). These findings demonstrate that IAA inhibits resistance plasmid spread by depleting PEP and blocking EI phosphorylation, thereby disrupting the PTS-cAMP-CRP signaling axis and restricting energy supply essential for T4SS function.

2.4. IAA targets enolase to deplete phosphoenolpyruvate

To identify the target mediating PEP depletion, we examined IAA effects on glycolytic enzymes converting 2-phosphoglycerate (2-PGA) to pyruvate (Fig. 5B). IAA exposure reduced mRNA levels of *eno* (enolase), *pykA* and *pykF* (pyruvate kinase isozymes) and concomitantly inhibited their enzymatic activities (Fig. 5E−G). Genetic dissection revealed that whereas *pykA* or *pykF* deletion minimally affected PEP pools, *eno* knockout substantially reduced intracellular PEP (Fig. 5H), indicating that enolase, not pyruvate kinase, represents the rate-limiting step controlling PEP availability.

Consistent with this, Δ*eno* strains exhibited decreased intracellular ATP and conjugative transfer frequency (Fig. 5I and J), phenocopying IAA treatment. We therefore investigated whether IAA directly inhibits enolase. Molecular docking predicted high-affinity binding (−4.96 kcal/mol) between IAA and enolase, with the ligand forming monodentate coordination with the catalytic Mg^{2+} and hydrogen bonds with Lys341, Lys392 and Asp245 (Fig. 5K). Surface plasmon resonance (SPR) analysis confirmed the direct interaction between IAA and enolase, with an equilibrium dissociation constant (K_D) of 76.5 μmol/L (Fig. 5L). Enzymatic assays further demonstrated concentration-dependent inhibition with a half-maximal inhibitory concentration (IC_{50}) of 68.7 μmol/L (12.07 μg/mL; 95% confidence interval: 6.42−16.96 μg/mL) (Fig. 5M). The close correspondence between K_D and IC_{50} values validates specific binding-mediated inhibition. Notably, this IC_{50} lies substantially below the MIC, confirming that IAA suppresses enolase at sub-lethal concentrations without affecting bacterial viability.

We next established the epistatic relationship between IAA and the glycolytic-phosphorelay pathway. In Δ*eno*, Δ*ptsI* and Δ*crp* backgrounds, conjugative transfer frequencies were already reduced relative to wild-type, and, critically, IAA treatment failed to further inhibit transfer in these mutants (Fig. 5N). This demonstrates that a functional *eno-ptsI-crp* pathway is epistatic to (*i.e.*, required for) IAA-mediated inhibition. Concordantly, we found that T4SS gene expression was downregulated in all three knockout strains, mirroring IAA effects (Fig. 5O). Collectively, these findings demonstrate that IAA inhibits conjugative transfer by directly binding enolase, thereby depleting PEP, blocking PTS-mediated phosphorylation signaling, and ultimately restricting ATP-dependent T4SS assembly.

2.5. IAA inhibits $FADH_2$ oxidation and reduces riboflavin production

Disruption of PTS phosphorylation redirects metabolic flux from glycolysis and the tricarboxylic acid (TCA) cycle toward the pentose phosphate pathway (PPP)[38]. Metabolomic analysis of donor bacteria revealed upregulated PPP activity following IAA treatment (Fig. 6A), accompanied by elevated enzymatic activities of glucose-6-phosphate dehydrogenase (G6PDH) and 6-phosphogluconate dehydrogenase (6PGDH) (Fig. 6B and C) and increased expression of PPP-associated genes *via* RT-qPCR analysis (Fig. 6D). These observations confirm that IAA impairs ATP production, with compensatory PPP upregulation proving insufficient to restore energy homeostasis, resulting in net ATP depletion.

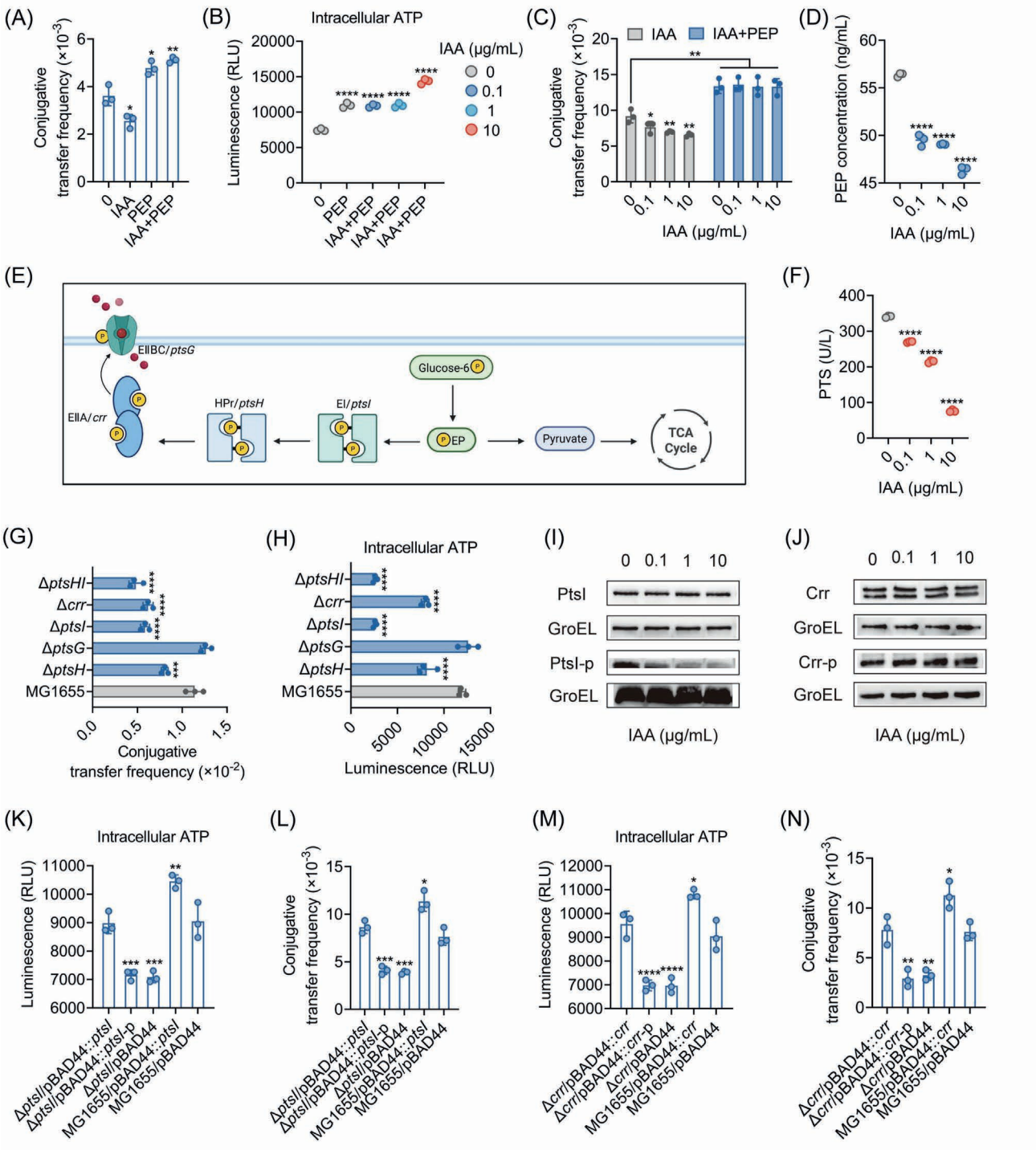

Figure 4 IAA inhibits the phosphotransferase system to block conjugation. (A) Frequency of conjugative transfer of RP4-7 plasmid in the presence of 10 μg/mL IAA, PEP, and 10 μg/mL IAA + PEP. (B) Intracellular ATP levels in donor bacteria upon exposure to various concentrations of IAA, PEP, and IAA + PEP. (C) Frequency of conjugative transfer of resistance plasmids upon exposure to different concentrations of IAA, PEP or IAA + PEP. (D) Intracellular PEP concentration of donor bacteria, detected using ELISA kits. (E) The schematic diagram of the phosphorylation and uptake of carbohydrates. (F) The activity of bacterial PTS after treatment with different concentrations of IAA. (G and H) Conjugative transfer frequency (G) and intracellular ATP levels (H) of MG1655, Δ*ptsH*, Δ*ptsG*, Δ*ptsI*, Δ*crr*, Δ*ptsHI* carrying RP4-7 plasmids. (I and J) The phosphorylation levels of *ptsI* (I) and *crr* (J) in bacteria treated with IAA. (K and L) Intracellular ATP levels (K) and frequency of conjugative transfer (L) in complemented strains Δ*ptsI*/pBAD44*ptsI*, H189Q phosphorylation site mutant Δ*ptsI*/pBAD44*ptsI*-p and overexpression strains MG1655/pBAD44*ptsI* of *ptsI*. (M and N) Intracellular ATP levels (M) and frequency of conjugative transfer (N) in complemented strains Δ*crr*/pBAD44*crr*, H91Q phosphorylation site mutant Δ*crr*/pBAD44*crr*-p and overexpression strains MG1655/pBAD44*crr* of *crr*. Data are presented as mean ± SD ($n = 3$). Statistical significance was determined by one-way ANOVA ($^{*}P < 0.05$, $^{**}P < 0.01$, $^{***}P < 0.001$, $^{****}P < 0.0001$).

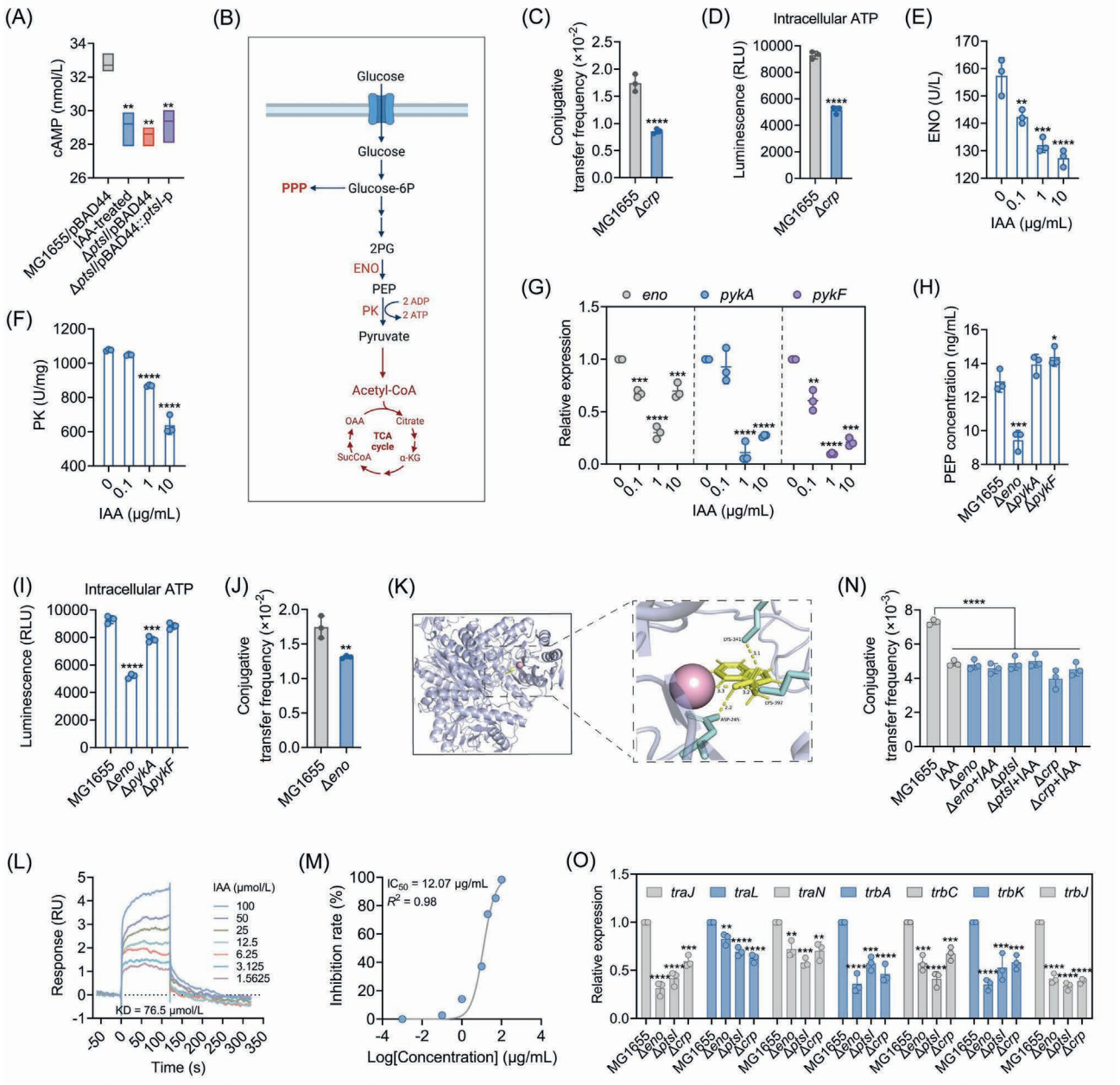

Figure 5 IAA targets enolase to reduce phosphoenolpyruvate levels. (A) Intracellular cAMP levels of donor bacteria treated with 10 μg/mL IAA, *ptsI* knockout strain Δ*ptsI*/pBAD44 and H189Q phosphorylation site mutant Δ*ptsI*/pBAD44*ptsI*-p. (B) The schematic diagram of glycolysis. (C, D) Conjugative transfer frequency (C) and intracellular ATP levels (D) of Δ*crp* carrying RP4-7 plasmid as a donor. (E, F) The activity of the critical enzyme enolase (ENO) (E) and pyruvate kinase (PK) (F). (G) RT-qPCR analysis of the relative expression of *eno*, a gene encoding enolase, and *pykA* and *pykF*, genes encoding pyruvate kinases. (H) Intracellular PEP content of MG1655, Δ*eno*, Δ*pykA*, and Δ*pykF* carrying RP4-7 plasmid. (I) Intracellular ATP levels of MG1655, Δ*eno*, Δ*pykA*, and Δ*pykF*. (J) Conjugative transfer frequency of *E. coli* MG1655 and Δ*eno* carrying RP4-7 plasmid. (K) Molecular docking analysis of IAA and protein enolase. (L) Surface plasmon resonance (SPR) analysis of the binding affinity of IAA with enolase. (M) The half-maximal inhibitory concentration (IC_{50}) of IAA against enolase activity. (N) Conjugative transfer frequency of Δ*eno*, Δ*ptsI*, and Δ*crp* carrying the RP4-7 plasmid after treatment with 10 μg/mL IAA. (O) T4SS-associated gene expression levels of Δ*eno*, Δ*ptsI*, and Δ*crp* carrying the RP4-7 plasmid. Data are presented as mean ± SD ($n = 3$). Statistical significance was determined by unpaired Student's *t*-test for two-group comparisons and one-way ANOVA for multiple-group comparisons ($^{*}P < 0.05$, $^{**}P < 0.01$, $^{***}P < 0.001$, $^{****}P < 0.0001$).

Reactive oxygen species (ROS) production has been proven to enhance the chromosomal recombination and promote conjugative transfer[41]. Because carbon flux through the PPP feeds into riboflavin biosynthesis, we investigated whether IAA modulates ROS *via* flavin metabolism. Riboflavin (vitamin B2) serves as the precursor for flavin mononucleotide (FMN) and flavin adenine dinucleotide (FAD), coenzymes essential for flavoprotein including succinate dehydrogenase (SDH)[42]. Autoxidation of

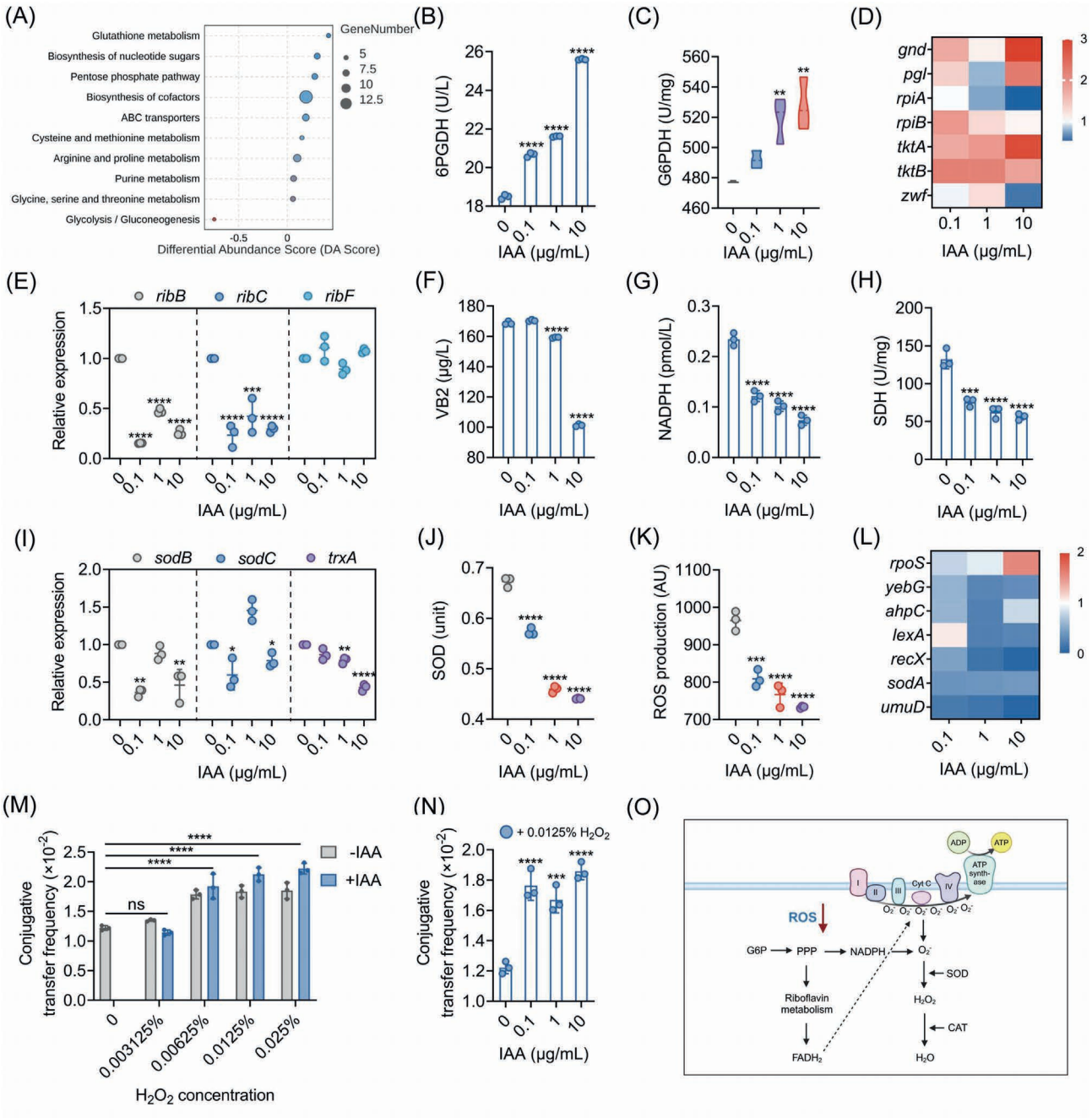

Figure 6 IAA inhibits $FADH_2$ oxidation and riboflavin biosynthesis. (A) Differential Abundance Score (DA Score) of key KEGG pathways in metabolomics analysis of donor bacteria. Scores 1 and −1 indicate trends of up- or down-regulation of expression of all annotated differential metabolites in the pathway, respectively. (B−D) The activity of 6-phosphogluconate dehydrogenase (6PGDH) (B) and glucose-6-phosphate dehydrogenase (G6PDH) (C) in the pentose phosphate pathway (PPP), and mRNA expression levels of related genes (D). (E) mRNA expression levels of the genes *ribB*, *ribC*, and *ribF*. (F) Intracellular concentration of riboflavin (VB2). (G) Intracellular levels of NADPH induced by IAA. (H) Succinate dehydrogenase (SDH) activity in donor bacteria after exposure to IAA. (I) Gene expression of antioxidant response pathways. (J) Superoxide dismutase (SOD) activity in the donor bacteria. (K) ROS production in the donor bacteria under IAA treatment for 1 h. (L) RT-qPCR analysis of the relative expression of ROS- and SOS response-related genes. (M) Conjugative transfer frequency of RP4-7 plasmid after supplementation of different concentrations of H_2O_2 in a conjugation system containing 10 μg/mL IAA. (N) Conjugative transfer frequency of RP4-7 plasmid after supplementation of 0.0125% H_2O_2 in conjugation systems containing different concentrations of IAA. (O) The schematic diagram of the reduction of ROS generation upon IAA treatment. Data are presented as mean ± SD ($n = 3$). Statistical significance was determined by unpaired Student's *t*-test for two-group comparisons and one-way ANOVA for multiple-group comparisons (*$P < 0.05$, **$P < 0.01$, ***$P < 0.001$, ****$P < 0.0001$; ns, not significant).

reduced FAD ($FADH_2$) generates superoxide (O_2^-) and hydrogen peroxide (H_2O_2), critical ROS sources (Fig. 6O)[43]. To investigate ROS production associated with riboflavin and $FADH_2$ oxidation, we initially measured the expression levels of *ribB*, *ribC*, and *ribF*, which function to convert 6,7-dimethyl-8-(D-ribityl) lumazine to riboflavin, riboflavin to FMN, and FMN to FAD, respectively. Consequently, IAA exposure significantly suppressed expression of *ribB* and *ribC* (Fig. 6E), leading to dose-dependent depletion of intracellular riboflavin (Fig. 6F). Concurrently, IAA diminished NADPH levels (Fig. 6G), compromising the reducing equivalents required for ROS detoxification and biosynthetic reactions[44]. Additionally, IAA inhibited SDH activity (Fig. 6H), thereby attenuating $FADH_2$ generation during succinate oxidation.

Consistent with reduced ROS production, IAA treatment decreased superoxide dismutase (SOD) activity (Fig. 6J) and downregulated expression of antioxidant genes (*trxA*, *sodB*, *sodC*) (Fig. 6I). Direct ROS measurements confirmed reduced oxidative stress (Fig. 6K), accompanied by downregulation of ROS- and SOS-response genes (Fig. 6L). Critically, exogenous H_2O_2 supplementation rescued conjugative transfer in IAA-treated cultures (Fig. 6M and N), suggesting that ROS limitation mechanistically underlies the inhibitory effect. Collectively, these results demonstrate that IAA suppresses resistance plasmid transfer by inhibiting riboflavin biosynthesis and $FADH_2$ oxidation, thereby attenuating ROS generation required for efficient conjugation.

2.6. IAA inhibits conjugation independently of proton motive force

To determine whether IAA-mediated ATP depletion results from membrane depolarization, we assessed proton motive force (PMF) and membrane integrity. In Gram-negative bacteria, the outer and inner membranes constitute barriers to plasmid transfer[45]. First, we measured variations in bacterial outer and inner membrane permeability using fluorescent probes 1-*N*-phenylnaphthylamine (NPN) and propidium iodide (PI), respectively. Consequently, we found that IAA treatment increased outer membrane permeability without affecting inner membrane integrity (Supporting Information Fig. S9A and S9B). Meanwhile, the expression levels of outer membrane proteins (OMPs)-related genes were increased upon IAA exposure (Supporting Information Fig. S8). Next, we determined membrane fluidity with a membrane-sensitive dye, Laurdan, which contacts phospholipids in cell membranes. The results showed that the fluorescence intensity was diminished as IAA concentrations increased, indicating enhanced membrane fluidity (Fig. S9C).

Membrane rigidity is implicated in bacterial membrane homeostasis, particularly the maintenance of PMF, which typically consists of the electrical potential ($\Delta\Psi$) and the transmembrane proton gradient (ΔpH), and can regulate conjugative transfer by impairing flagellar motility and energy metabolism[46]. We evaluated the effects of IAA on bacterial ΔpH and $\Delta\Psi$ using fluorescent probes BCECF-AM and $DiSC_3(5)$, respectively. However, no significant fluorescence intensity changes were observed (Fig. S9D and S9E). Consistently, flow cytometric analysis confirmed stable PMF in IAA-treated cells compared with carbonyl cyanide m-chlorophenylhydrazone (CCCP)-treated positive controls (Fig. S9F).

Because flagellar motility depends strictly on PMF, we further validated PMF integrity functionally. Swimming assays demonstrated unaltered motility in IAA-treated bacteria (Supporting Information Fig. S10), confirming that electrochemical potential remains intact. These results indicate that IAA enhances outer membrane permeability and fluidity but preserves transmembrane electrochemical potential. The inhibition of conjugative transfer therefore occurs independently of PMF dissipation, ruling out membrane depolarization as the mechanism underlying ATP depletion.

2.7. IAA prevents plasmid transfer in vivo

To validate the physiological relevance of our *in vitro* findings, we assessed IAA efficacy in a murine infection model. CD-1 mice received intraperitoneal co-inoculation of *E. coli* DH5α (donor) and *E. coli* EC600 (recipient) at a 1:1 ratio, followed 15 min later by intraperitoneal administration of either PBS (vehicle) or IAA (0.5 mg/kg) (Fig. 7A). After 24 h, bacterial loads in liver and spleen were quantified. The results indicated that IAA treatment significantly reduced conjugative transfer frequencies in both liver and spleen compared with vehicle controls (Fig. 7B and D). Importantly, recipient bacterial counts remained unchanged (Fig. 7C and E), confirming that the reduction in transconjugants resulted from inhibition of plasmid transfer rather than bacterial killing or growth suppression. These results demonstrate that IAA effectively prevents horizontal dissemination of antibiotic resistance plasmids *in vivo* at sub-bactericidal concentrations.

3. Discussion

The escalating antimicrobial resistance crisis necessitates alternative strategies that circumvent the selective pressure driving resistance evolution[47]. HGT inhibitors offer a compelling chemoprophylactic approach by suppressing resistance dissemination without imposing bactericidal selection. Indoles, naturally abundant aza-heterocyclic compounds, exhibit diverse biological activities, including antitumor and anti-inflammatory effects[48]. Our study identified indole derivatives as potent conjugation inhibitors and elucidated a structure−activity relationship governed by electron-withdrawing group positioning. This aligns with prior studies highlighting the impact of side-chain modifications on their biochemical properties[49]. For instance, studies on modifying C2, C3, and C5 positions of the indole scaffold while retaining an electron-withdrawing group led to the discovery of effective NorA inhibitors[50,51]. The presence of electron-withdrawing groups increases the acidity and decreases the basicity of a compound[52], suggesting that increased acidity in indoles may strengthen their ability to inhibit plasmid conjugation. Given that unsaturated fatty acids (*e.g.*, oleic and linoleic acids) similarly inhibit HGT, we reasoned that optimizing the electronic properties of indole analogues may yield superior clinical candidates[8,53]. Future structure-based drug design should focus on refining these substituent effects to enhance target engagement while maintaining biocompatibility.

The bacterial PTS coordinates carbon metabolism, nutrient sensing and energy status, thereby governing diverse physiological processes including virulence and motility[54,55]. These regulatory functions are mediated through phosphoryl-transfer signals among PTS components[56], utilizing PEP as the obligate phosphoryl donor to drive substrate uptake and phosphorylation[57]. Although historically characterized as a carbohydrate transport apparatus, the PTS fundamentally couples nutrient availability to energy metabolism. Previous studies have demonstrated that metabolic flux

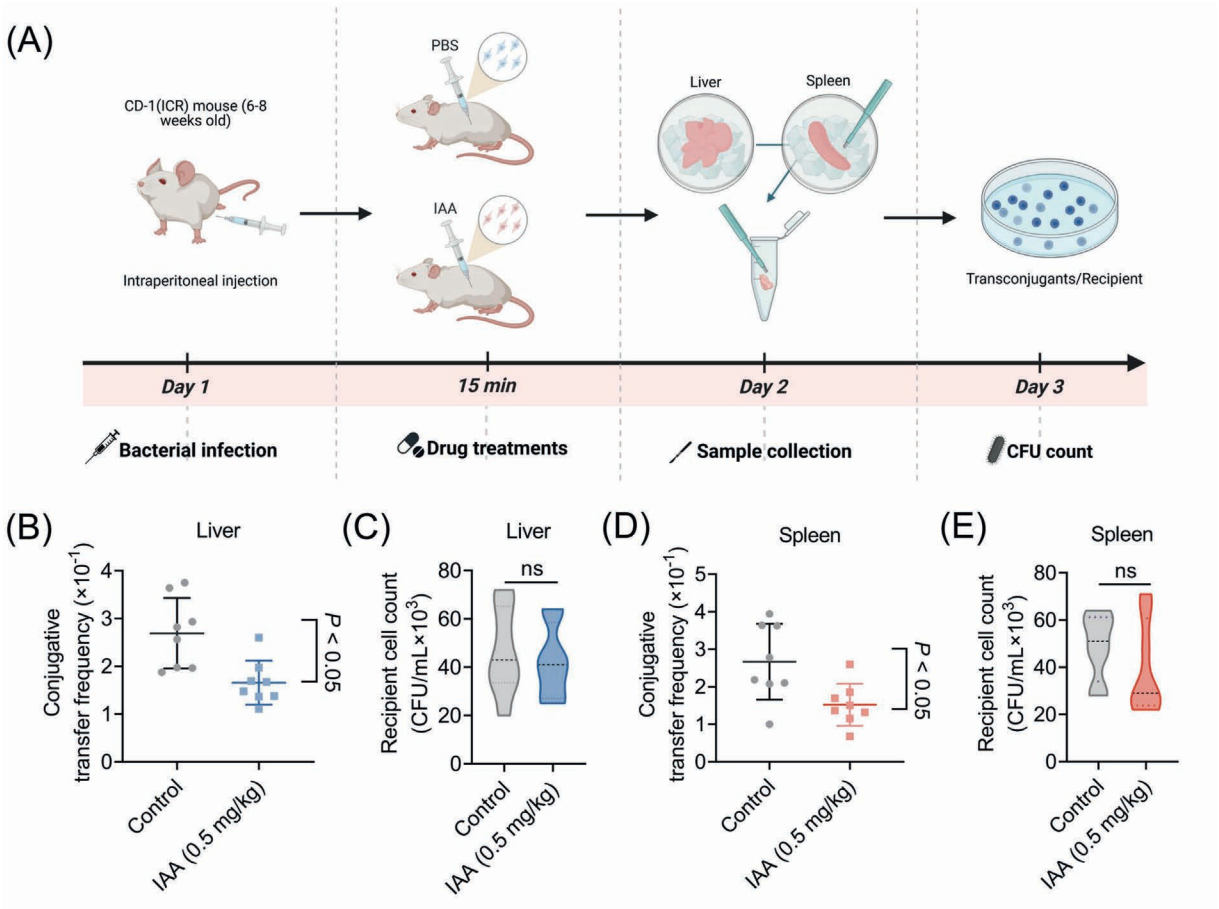

Figure 7 IAA inhibits conjugative transfer *in vivo*. (A) Schematic diagram of experimental protocol for the animal trial. (B−E) The conjugative transfer frequency and the number of recipient bacteria in the liver (B, C) and spleen (D, E). Data are presented as mean ± SD (n = 8). P values were determined by Mann−Whitney U test. ns, not significant.

redistribution, such as phenol-induced carbon flux diversion through *ptsI* defects away from the TCA cycle and glycolysis toward the PPP, directly impacts bacterial physiology[38]. Given that conjugative DNA transfer requires both ATP and PMF[58], and considering the structural and functional parallels between VirB10-like conjugation subunits and TonB-family energy transducers[59], we hypothesized that PTS-mediated energy transduction, rather than simple sugar import, constitutes a critical determinant of plasmid conjugation efficiency. Our findings validate this hypothesis, revealing an unanticipated role for the PTS phosphorylation cascade as a metabolic checkpoint governing horizontal gene transfer. Specifically, maintenance of intracellular ATP pools through PTS phosphoryl-relay activity proves essential for conjugative DNA transfer, positioning the PTS as a regulatory node that couples energy status to plasmid transfer.

Our mechanistic studies identify enolase as the primary molecular target of IAA. By inhibiting enolase-catalyzed 2-phosphoglycerate conversion, IAA depletes PEP, the obligate phosphoryl donor for PTS initiation[60]. This establishes a hierarchical suppression cascade wherein enolase inhibition depletes PEP, consequently blocking PTS phosphorylation and redirecting metabolic flux toward the PPP[38], ultimately limiting ATP availability. The observation that *ptsG* knockout (ablating glucose transport but preserving phosphoryl relay) does not impair conjugation confirms that energy deprivation, rather than nutrient uptake failure, underlies the inhibitory mechanism. Furthermore, reduced $FADH_2$ oxidation and diminished ROS generation, consequences of respiratory chain suppression[61], cooperate with ATP depletion to arrest T4SS function (Fig. 8).

Notably, we observed a biphasic response wherein low-dose IAA promoted while high-dose IAA inhibited transfer of *mcr-1*-bearing plasmids. This mirrors previously reported biphasic response in conjugation systems exposed to phenolic compounds[62]. We hypothesized that subthreshold ATP reduction may trigger compensatory metabolic adaptations that inadvertently enhance conjugation efficiency, potentially through stress-induced SOS response modulation or stringent response activation. The specificity of this effect for *mcr-1* plasmids, despite the inherent fitness cost of colistin resistance[63], suggests plasmid-encoded regulatory elements may differentially modulate host energy sensing. Further investigation is required to delineate the molecular determinants of this dose-dependent paradox.

While our intraperitoneal infection model demonstrates IAA efficacy in preventing resistance spread *in vivo*, the gastrointestinal tract represents the predominant reservoir for HGT and resistance evolution. Translation to clinical practice necessitates validation in enteric colonization models using oral administration routes to assess bioavailability, microbiome perturbation and prophylactic efficacy against gut-borne resistance transmission. Further studies using intestinal models will be conducted in our

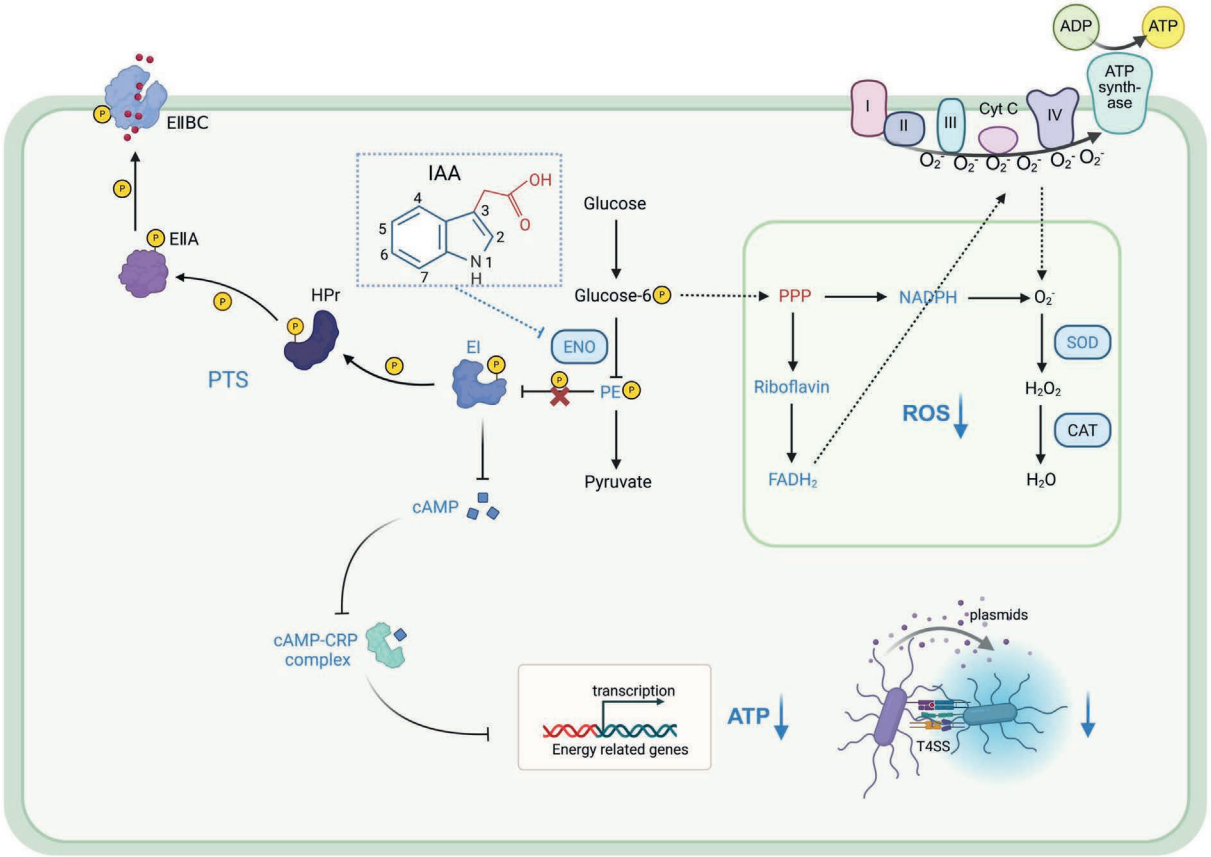

Figure 8 Schematic diagram of the molecular mechanism by which IAA suppresses horizontal transfer of resistance plasmids. Red means up, and blue means down.

future work to obtain more clinically relevant results. Moreover, the favorable safety profile of IAA, a naturally occurring microbiota metabolite and plant hormone, supports its development as a prophylactic agent to prevent nosocomial transmission of multidrug-resistant pathogens.

In conclusion, our work establishes metabolic targeting of the enolase-PTS-cAMP axis as a viable strategy to combat antibiotic resistance propagation. By uncoupling resistance suppression from bacterial viability, IAA and related indole derivatives offer a paradigm for 'anti-evolution' therapeutics that preserve antimicrobial efficacy by restricting HGT. These findings provide a mechanistic foundation for developing next-generation adjuvants that protect antibiotic utility through chemical inhibition of plasmid transfer.

4. Experimental

4.1. Bacterial strains, culture conditions and drugs

In this study, *E. coli* DH5α carrying the RP4-7 plasmid, which confers resistance to ampicillin (AMP) and chloramphenicol (CAP), was used as the donor strain. The recipient bacteria were *E. coli* EC600, which is resistant to rifampicin (Rif). Indole compounds were purchased from Shanghai Yuanye Bio-Technology, and antibiotics were supplied by the China Institute of Veterinary Drug Control. Unless otherwise stated, bacteria were cultured routinely in Luria-Bertani (LB) medium. A complete list of bacterial strains and plasmids utilized in this study was presented in Supporting Information Tables S2 and S3.

4.2. Animal studies and ethical statement

Female CD-1 mice (6−8 weeks old; 20−25 g) were sourced from the Comparative Medicine Center of Yangzhou University. All animal experiments followed the guidelines of Jiangsu Laboratory Animal Welfare and Ethical Committee of Jiangsu Administrative Committee of Laboratory Animals. The protocols were approved by the Jiangsu Laboratory Animals Administrative Committee under license number SYXK-2022-0044. The laboratory animal usage license number SCXK-2022-0009 was certified by the Jiangsu Association for Science and Technology.

4.3. Conjugation assays

E. coli DH5α and *E. coli* EC600 were grown in LB broth at 37 °C as donor and recipient respectively, followed by collection through centrifugation. Subsequently, the bacterial precipitates were suspended in LB broth and the optical density OD_{600} was adjusted to 0.25. Equal volumes of donor and recipient cultures (1 mL each) were mixed with indole compounds and incubated at 37 °C with shaking at 200 rpm for 15 h. After incubation, agar plates with the appropriate antibiotics were employed to screen for recipient and transconjugants, and the conjugative transfer frequency was calculated by dividing the number of transconjugants by the

recipient bacteria. In addition, subsequent conjugation assays were performed using clinical isolates carrying the bla_{NDM-5}, *tet*(X4) and *mcr-1* plasmids[64].

4.4. LC−MS analysis

Bacterial cultures were co-incubated with IAA for a duration of 8 h. Subsequently, the bacterial precipitates were rapidly cryopreserved using liquid nitrogen and stored at −80 °C. Briefly, the cell pellets were subjected to extraction in 500 μL of methanol, which contained 0.1 mg/L trimethoprim, 0.1 mg/L nortriptyline, and 0.3 mg/L glipizide as internal standards. This extraction process involved vigorous shaking and sonication. The resulting extracts were then separated from the solid matter *via* centrifugation. A volume of 400 μL from each extract was evaporated to dryness and subsequently reconstituted in 40 μL of a 50% (*v*/*v*) acetonitrile solution containing 0.1% formic acid, with the addition of 1 mg/L caffeine and 8 mg/L naproxen serving as internal standards. An aliquot of 1 μL from each sample was subjected to analysis *via* reversed-phase ultra-high performance liquid chromatography (UHPLC) coupled with quadrupole time-of-flight mass spectrometry (Q-TOF MS). Tandem mass spectra were obtained from pooled quality control samples and utilized for metabolite identification through comparison with authentic standards and/or metabolite databases, as previously described. The LC−MS data were exported to mzXML format using Bruker Compass Xport and subsequently preprocessed using XCMS Online. Following preprocessing, the untargeted metabolomics data were further analyzed using R/RStudio, employing the 'tidyverse' suite of packages for statistical analysis[65].

4.5. Respiration measurement

Bacterial suspensions were cultured to the logarithmic growth phase, along with IAA and the fluorescent probe resazurin (0.1 μg/mL), were aliquoted into black 96-well plates. Fluorescence changes were monitored continuously over a period of 1 h, utilizing excitation and emission wavelengths of 550 and 590 nm, respectively.

4.6. Intracellular ATP determination

Intracellular ATP levels were quantified utilizing the Enhanced ATP Assay Kit (Beyotime, Shanghai, China). Bacterial cultures were cultivated to the logarithmic phase and subsequently washed with PBS and adjusted to an OD_{600} of 0.25. Thereafter, the bacteria were incubated with varying concentrations of IAA for 1 h. Centrifugation was performed to remove the supernatant, and bacterial cells were lysed using a lysis solution. Luminescence signals were then measured to determine intracellular ATP levels.

4.7. RNA extraction and RT-qPCR analysis

Donor and recipient bacteria were cultured to logarithmic phase, and the OD_{600} was adjusted to 0.25. Bacteria were incubated with IAA for 4 h. Total RNA was then extracted and quantified using a Nanodrop spectrophotometer (Thermo Scientific). The extracted RNA was then reverse transcribed into cDNA utilizing the HiScript® III RT SuperMix for qPCR (+gDNA wiper) Kits (Vazyme). The reverse transcription-quantitative polymerase chain reaction (RT-qPCR) analysis was performed using the 7500 Fast Real-Time PCR System (Applied Biosystems, CA, USA) in conjunction with ChamQ™ SYBR® Color qPCR Master Mix Kits (Vazyme Biotech, China). 16S rRNA gene was employed as a reference gene to determine the relative fold change in mRNA expression. The primer sequences required for the analysis are listed in Supporting Information Table S4.

4.8. Construction of knockout mutants

The knockout mutants of genes *cydB*, *mdh*, *ptsI*, *ptsH*, *ptsG*, *crr*, *ptsHI*, *eno*, *pykA*, *pykF* and *crp* were constructed based on an allelic exchange strategy. The suicide plasmid pRE112 was linearized using two restriction enzymes (QuickCut XbaI and XmaI). The upstream and downstream 500 bp fragments of the gene to be knocked out were amplified by PCR using *E. coli* MG1655 as a template. The digested products were separated by agarose gel electrophoresis and purified using Omega Cycle Pure Kit. Amplified upstream and downstream fragments were assembled into linearized plasmids and ligated to suicide plasmids *in vitro* using the ClonExpress Ultra Single Step Cloning Kit. The ligated plasmids were used to transform chemically competent *E. coli* DH5α cells and verify positive clones by DNA sequencing. Allelic exchange vectors in positive clones were isolated and purified using the Omega Plasmid Mini Kit according to the manufacturer's instructions. Subsequently, the purified allele exchange vector was electro-transformed into *E. coli* X7213. *E. coli* X7213 was employed as the donor and *E. coli* MG1655 as the recipient for conjugative transfer. Finally, LB agar plates containing 15% sucrose were used for the selection of double-crossover mutants[66]. All primers employed are listed in Table S4.

4.9. Measurement of the intracellular PEP, PTS, VB2, cAMP and enolase

ELISA kits were utilized to determine bacterial intracellular conditions of phosphoenolpyruvate (PEP), phosphotransferase system (PTS), riboflavin (VB2), cyclic adenosine monophosphate (cAMP) and enolase (ENO). Bacteria were cultured until reaching logarithmic phase and treated with IAA for 4 h. The bacteria were then sonicated on ice for 5 min, followed by centrifugation for 5 min to discard the supernatant. Samples and standards were loaded onto the ELISA plate, and 100 μL of horseradish peroxidase (HRP)-conjugated antibody was added to each well. The reaction proceeded for 60 min at 37 °C. After completion, the plate was washed five times with washing solution. Subsequently, 50 μL of substrates A and substrates B were added to each well and incubated for 15 min at 37 °C in the dark. Finally, 50 μL of stop solution was added to each well, and the absorbance at 450 nm was measured using a microplate reader.

4.10. Western blot analysis

The *crr*-FLAG and *ptsI*-FLAG genes were amplified from *E. coli* MG1655 using the primers listed in Table S4 and cloned into the expression vector pBAD44 between the XhoI/EcoRI sites. The plasmid was constructed in *E. coli* DH5α and electroporated into *E. coli* MG1655. The constructed plasmids were confirmed by PCR and sequencing. Bacterial cells were disrupted using TieChui *E. coli* Lysis Buffer. A total of 5 μL of protein was loaded into the Phos-tag protein gel. The isolated proteins were blotted onto a polyvinylidene difluoride membrane according to the manufacturer's instructions. Immunoblotting was performed with HRP-conjugated FLAG monoclonal antibody for 2 h at room

temperature. After washing the membrane with TBS containing 0.05% Tween 20, bound antibody was detected with Super Signal West Pico PLUS Chemiluminescent Substrate and ChemiDoc MP Imaging System[67].

4.11. Construction of point mutations in ptsI and crr genes

The phosphorylation site at amino acid residue 91 of the *crr* gene and phosphorylation site at amino acid residue 189 of *ptsI* were point mutated using a two-step PCR method. Briefly, the first round of PCR was performed using primers *ptsI*-N, *ptsI*-P and *crr*-N, *crr*-P. After the first PCR step, the quantity and quality of the PCR products were checked on a 2% agarose gel. The fragments were purified using Omega Cycle Pure Kit. An aliquot of each fragment purified from the first PCR amplification was prepared as the template for the next reaction with primers. The plasmid pBAD44 was linearized using two restriction enzymes (QuickCut XhoI and EcoRI). The purified second round of PCR product was ligated to the pBAD44 plasmid with the ClonExpress Ultra Single Step Cloning Kit. The mutation was confirmed in the selected colonies by Sanger sequencing. The recombinant vectors were electrotransformed into *crr* and *ptsI* knockout strains[68].

4.12. Construction of complemented and overexpression strains

The method was the same as for the construction of point mutant strains. For the complemented strains, recombinant vectors ligated with the target gene fragments were transformed into the knockout strains. For overexpression strains, the recombinant vectors were electroporated into *E. coli* MG1655.

4.13. Enzyme activity assay

Enzyme activities were quantified by pyruvate kinase (PK), 6-phosphogluconate dehydrogenase (6PGDH), and glucose-6-phosphate dehydrogenase (G6PDH) Activity Assay Kits. In brief, bacterial cultures were collected, washed, resuspended with PBS, and adjusted to an OD_{600} of 0.25. Aliquots of 1 mL samples were sonicated for 5 min, and the resulting supernatant was used for detection.

4.14. Docking analysis

A template was created using the crystal structure of the enolase protein (PDB accession number: 6BFZ). Enolase and IAA were molecularly docked using the MaxFlow tool without the use of water molecules. In a 2D graphic, PyMOL was applied to depict the interactions of IAA with the residues of the binding sites in enolase.

4.15. Surface plasmon resonance (SPR) analysis

The CM5 sensor chip surface was initially activated through a 7-min injection (flow rate: 10 μL/min) of freshly prepared 400 mmol/L EDC/100 mmol/L NHS mixture. Following activation, enolase solution (50 μg/mL in immobilization buffer) was introduced into the sample channel at a flow rate of 10 μL/min for covalent immobilization. For analyte binding analysis, IAA solutions were serially diluted in analyte buffer to generate seven concentration gradients (1.5625−100 μmol/L). Each analyte solution was perfused through the flow cells at 30 μL/min flow rate, maintaining 120 s association phase followed by 300 s dissociation phase. The concentration series was sequentially injected in ascending order through seven complete regeneration cycles. Post-injection regeneration was achieved using 10 mmol/L Glycine−HCl (pH 2.0) at 30 μL/min flow rate for 30 s, effectively removing bound analytes while preserving ligand integrity. All binding experiments were conducted under continuous analyte buffer perfusion at 25 °C.

4.16. Half-maximal inhibitory concentration (IC_{50}) determination

To determine the inhibitory activity of IAA against enolase, purified enolase (20 nmol/L) was preincubated with a range of IAA concentrations in assay buffer (50 mmol/L Tris, pH 8.0, 0.1 mol/L KCl, 1 mmol/L $MgSO_4$) for 5 min at room temperature. The enzymatic reaction was initiated by adding 2-phosphoglycerate to a final concentration of 1.0 mmol/L. The absorbance at 240 nm was continuously monitored to calculate the initial reaction rate. All experiments were performed in triplicate, and the half-maximal inhibitory concentration (IC_{50}) was determined by fitting the dose-response curve to a four-parameter logistic model[69].

4.17. SOD activity determination

The intracellular superoxide dismutase (SOD) activity in bacteria was assessed following treatment with IAA at various concentrations, utilizing the Total Superoxide Dismutase Assay Kit with WST-8 (Beyotime, Shanghai, China).

4.18. ROS determination

Intracellular levels of reactive oxygen species (ROS) were quantified using the fluorescent probe DCFH-DA (10 μmol/L). Bacteria were co-incubated with DCFH-DA (10 μmol/L) for a duration of 30 min. Unbound DCFH-DA was removed by washing with PBS, after which 190 μL of bacteria and 10 μL of IAA were added to a black 96-well plate. Fluorescence intensity was assessed by measuring excitation at 488 nm and emission at 525 nm.

4.19. Membrane permeability and fluidity assay

The permeability and fluidity of bacterial membranes were assessed using 1-*N*-phenylnaphthylamine (NPN), propidium iodide (PI) and Laurdan, respectively. Co-incubation of fluorescent dye and bacteria was maintained for 30 min and then different concentrations of IAA were introduced into black 96-well plates. Measurements were performed with a microplate reader, NPN at 350/420 nm, PI at 535/615 nm, and Laurdan fluorescence levels at 435 and 490 nm emission and 350 nm excitation wavelengths.

4.20. Proton motive force (PMF) detection

The fluorescence probes BCECF-AM (1 μmol/L) and 3,3′-dipropylthiadicarbocyanine iodide ($DiSC_3(5)$, 0.5 μmol/L) were employed to monitor pH fluctuations (ΔpH) and membrane potential variations ($\Delta\Psi$). Bacteria were incubated with the fluorescent probe for 30 min at 37 °C, and then different concentrations of IAA were incorporated. Changes in fluorescence intensity were recorded continuously for 1 h using a microplate reader.

The bacterial suspension was processed with IAA and CCCP for 1 h. Then, the bacteria were incubated with 3,3′-diethyl-oxo-iodocarbocyanine ($DiOC_2(3)$, 3 mmol/L) for 30 min away from light. The proton motive force was monitored with a CytExpert Flow Cytometer[70].

4.21. *In vivo study*

Donor and recipient bacteria were cultured overnight to an optical density at 600 nm of 0.5. Female CD-1 mice, aged 6−8 weeks, received intraperitoneal injections of 100 μL of the donor and recipient bacterial cultures. At 15 min post-infection, PBS and IAA at a concentration of 0.5 mg/kg were administered intraperitoneally. After 24 h, the spleen and liver of the mice were harvested, homogenized, and serially diluted. These samples were then analyzed for the presence of recipient bacteria and transconjugants using agar plates containing rifampicin (Rif) and a combination of rifampicin and ampicillin (Rif/AMP), respectively.

4.22. *Statistical analysis*

Statistical analysis was conducted using GraphPad Prism version 9.0 software. The data were acquired from a minimum of three biological replicates and expressed as mean ± SD. Unpaired Student's *t*-tests (for normally distributed data) were employed to compare two groups, while one-way ANOVA was used to compare multiple groups. Differences with a P value less than 0.05 were considered statistically significant. The level of significance was denoted by asterisks, with $*P< 0.05$, $**P< 0.01$, $***P< 0.001$ and $****P< 0.0001$.

Acknowledgments

This work was supported by National Natural Science Foundation of China (32222084), Key R&D Program of Jiangsu Province (Modern Agriculture) (BE2023332), Jiangsu Agricultural Science and Technology Innovation Fund (CX(24)3072), Jiangsu Postgraduates Practical Innovation Project (SJCX23_2012), A Project Funded by the Priority Academic Program Development of Jiangsu Higher Education Institutions (PAPD) and 111 Project D18007.

Author contributions

Yuan Liu: Conceptualization, Supervision, Funding acquisition, Writing-review & editing. Zhiqiang Wang: Investigation, Funding acquisition, Writing-review & editing. Miao Zhang: Investigation, Formal analysis, Writing-original draft. Bingqing Yang: Investigation, Writing-original draft. Jingyi Sun: Investigation, Visualization.

Conflicts of interest

The authors declare no conflict of interest.

Appendix A. Supporting information

Supporting information to this article can be found online at https://doi.org/10.1016/j.apsb.2026.04.021.

References

1. San Millan A. Evolution of plasmid-mediated antibiotic resistance in the clinical context. *Trends Microbiol* 2018;**26**:978−85.
2. Benz F, Huisman JS, Bakkeren E, Herter JA, Stadler T, Ackermann M, et al. Plasmid- and strain-specific factors drive variation in ESBL-plasmid spread *in vitro* and *in vivo*. *ISME J* 2021;**15**:862−78.
3. Loftie-Eaton W, Yano H, Burleigh S, Simmons RS, Hughes JM, Rogers LM, et al. Evolutionary paths that expand plasmid host-range: implications for spread of antibiotic resistance. *Mol Biol Evol* 2016; **33**:885−97.
4. Davies J, Davies D. Origins and evolution of antibiotic resistance. *Microbiol Mol Biol Rev* 2010;**74**:417−33.
5. Wailan AM, Sartor AL, Zowawi HM, Perry JD, Paterson DL, Sidjabat HE. Genetic contexts of bla_{NDM-1} in patients carrying multiple NDM-producing strains. *Antimicrob Agents Chemother* 2015;**59**: 7405−10.
6. Liu YY, Zhou Q, He W, Lin Q, Yang J, Liu JH. *mcr-1* and plasmid prevalence in *Escherichia coli* from livestock. *Lancet Infect Dis* 2020; **20**:1126.
7. He T, Wang R, Liu D, Walsh TR, Zhang R, Lv Y, et al. Emergence of plasmid-mediated high-level tigecycline resistance genes in animals and humans. *Nat Microbiol* 2019;**4**:1450−6.
8. Fernandez-Lopez R, Machon C, Longshaw CM, Martin S, Molin S, Zechner EL, et al. Unsaturated fatty acids are inhibitors of bacterial conjugation. *Microbiology* 2005;**151**:3517−26.
9. Li G, Xia LJ, Zhou SY, Wang XR, Cui CY, He YZ, et al. Linoleic acid and alpha-linolenic acid inhibit conjugative transfer of an IncX4 plasmid carrying *mcr-1*. *J Appl Microbiol* 2021;**130**:1893−901.
10. Poole TL, McReynolds JL, Edrington TS, Byrd JA, Callaway TR, Nisbet DJ. Effect of flavophospholipol on conjugation frequency between *Escherichia coli* donor and recipient pairs *in vitro* and in the chicken gastrointestinal tract. *J Antimicrob Chemother* 2006;**58**: 359−66.
11. Paschos A, den Hartigh A, Smith MA, Atluri VL, Sivanesan D, Tsolis RM, et al. An *in vivo* high-throughput screening approach targeting the type IV secretion system component VirB8 identified inhibitors of *Brucella abortus* 2308 proliferation. *Infect Immun* 2011; **79**:1033−43.
12. Makabenta JMV, Nabawy A, Li CH, Schmidt-Malan S, Patel R, Rotello VM. Nanomaterial-based therapeutics for antibiotic-resistant bacterial infections. *Nat Rev Microbiol* 2021;**19**:23−36.
13. Shaffer CL, Good JA, Kumar S, Krishnan KS, Gaddy JA, Loh JT, et al. Peptidomimetic small molecules disrupt type IV secretion system activity in diverse bacterial pathogens. *mBio* 2016;**7**. e00221-16.
14. Wu Y, Yan H, Zhu X, Liu C, Chu C, Zhu X, et al. Biochar effectively inhibits the horizontal transfer of antibiotic resistance genes *via* restraining the energy supply for conjugative plasmid transfer. *Environ Sci Technol* 2022;**56**:12573−83.
15. Xu Z, Li S, Ma Y, Li C, Lu H, Xiong J, et al. Role of organophosphorus pesticides in facilitating plasmid-mediated conjugative transfer: efficiency and mechanisms. *J Hazard Mater* 2025;**487**:137318.
16. Getino M, Sanabria-Rios DJ, Fernandez-Lopez R, Campos-Gomez J, Sanchez-Lopez JM, Fernandez A, et al. Synthetic fatty acids prevent plasmid-mediated horizontal gene transfer. *mBio* 2015;**6**:e01032-15.
17. Jia Y, Zheng Z, Yang B, Zhang H, Wang Z, Liu Y. A broad-spectrum horizontal transfer inhibitor prevents transmission of plasmids carrying multiple antibiotic resistance genes. *Transbound Emerg Dis* 2024;**2024**:7063673.
18. Shirinzadeh H, Suzen S, Altanlar N, Westwell AD. Antimicrobial activities of new indole derivatives containing 1,2,4-triazole, 1,3,4-thiadiazole and carbothioamide. *Turk J Pharm Sci* 2018;**15**:291−7.
19. Kumar S. Ritika. A brief review of the biological potential of indole derivatives. *Future J Pharmaceut Sci* 2020;**6**:121.
20. Chant EL, Summers DK. Indole signalling contributes to the stable maintenance of *Escherichia coli* multicopy plasmids. *Mol Microbiol* 2007;**63**:35−43.

21. Lee J, Jayaraman A, Wood TK. Indole is an inter-species biofilm signal mediated by SdiA. *BMC Microbiol* 2007;**7**:42.
22. Lee JH, Kim YG, Kim CJ, Lee JC, Cho MH, Lee J. Indole-3-acetaldehyde from *Rhodococcus* sp. BFI 332 inhibits *Escherichia coli* O157:H7 biofilm formation. *Appl Microbiol Biotechnol* 2012;**96**: 1071−8.
23. Lee JH, Lee J. Indole as an intercellular signal in microbial communities. *FEMS Microbiol Rev* 2010;**34**:426−44.
24. Liu Y, Yang K, Jia Y, Shi J, Tong Z, Fang D, et al. Gut microbiome alterations in high-fat-diet-fed mice are associated with antibiotic tolerance. *Nat Microbiol* 2021;**6**:874−84.
25. Jia Y, Yang B, Shi J, Fang D, Wang Z, Liu Y. Melatonin prevents conjugative transfer of plasmid-mediated antibiotic resistance genes by disrupting proton motive force. *Pharmacol Res* 2022;**175**:105978.
26. Xiong R, Liu Y, Pu J, Liu J, Zheng D, Zeng J, et al. Indole inhibits IncP-1 conjugation system mainly through promoting *korA* and *korB* expression. *Front Microbiol* 2021;**12**:628133.
27. Wang G, Fan Y, Zhang G, Cai S, Ma Y, Yang L, et al. Microbiota-derived indoles alleviate intestinal inflammation and modulate microbiome by microbial cross-feeding. *Microbiome* 2024;**12**:59.
28. Arabova L, Chumikina L, Arabov R, Topunov A. Indolyl-3-acetic acid for medical use. *Appl Biochem Microbiol* 2024;**60**:993−1009.
29. Chen I, Christie PJ, Dubnau D. The ins and outs of DNA transfer in bacteria. *Science* 2005;**310**:1456−60.
30. Guo J, Qiu X, Xie YG, Hua ZS, Wang Y. Regulation of intracellular process by two-component systems: exploring the mechanism of plasmid-mediated conjugative transfer. *Water Res* 2024;**259**:121855.
31. Siebold C, Flukiger K, Beutler R, Erni B. Carbohydrate transporters of the bacterial phosphoenolpyruvate: sugar phosphotransferase system (PTS). *FEBS Lett* 2001;**504**:104−11.
32. Deutscher J, Ake FM, Derkaoui M, Zebre AC, Cao TN, Bouraoui H, et al. The bacterial phosphoenolpyruvate: carbohydrate phosphotransferase system: regulation by protein phosphorylation and phosphorylation-dependent protein−protein interactions. *Microbiol Mol Biol Rev* 2014;**78**:231−56.
33. Deutscher J, Francke C, Postma PW. How phosphotransferase system-related protein phosphorylation regulates carbohydrate metabolism in bacteria. *Microbiol Mol Biol Rev* 2006;**70**:939−1031.
34. Gabor E, Gohler AK, Kosfeld A, Staab A, Kremling A, Jahreis K. The phosphoenolpyruvate-dependent glucose-phosphotransferase system from *Escherichia coli* K-12 as the center of a network regulating carbohydrate flux in the cell. *Eur J Cell Biol* 2011;**90**:711−20.
35. Doucette CD, Schwab DJ, Wingreen NS, Rabinowitz JD. alpha-Ketoglutarate coordinates carbon and nitrogen utilization *via* enzyme I inhibition. *Nat Chem Biol* 2011;**7**:894−901.
36. Huang K, Kapadia G, Zhu PP, Peterkofsky A, Herzberg O. A promiscuous binding surface: crystal structure of the IIA domain of the glucose-specific permease from *Mycoplasma capricolum*. *Structure* 1998;**6**:697−710.
37. Teplyakov A, Lim K, Zhu PP, Kapadia G, Chen CC, Schwartz J, et al. Structure of phosphorylated enzyme I, the phosphoenolpyruvate:sugar phosphotransferase system sugar translocation signal protein. *Proc Natl Acad Sci U S A* 2006;**103**:16218−23.
38. Zeng J, Hong Y, Zhao N, Liu Q, Zhu W, Xiao L, et al. A broadly applicable, stress-mediated bacterial death pathway regulated by the phosphotransferase system (PTS) and the cAMP-Crp cascade. *Proc Natl Acad Sci U S A* 2022;**119**:e2118566119.
39. Starcic M, Zgur-Bertok D, Jordi BJ, Wösten MM, Gaastra W, van Putten JP. The cyclic AMP-cyclic AMP receptor protein complex regulates activity of the *traJ* promoter of the *Escherichia coli* conjugative plasmid pRK100. *J Bacteriol* 2003;**185**:1616−23.
40. Harkova LG, de Dios R, Rubio-Valle A, Pérez-Pulido AJ, McCarthy RR. Cyclic AMP is a global virulence regulator governing inter and intrabacterial signalling in *Acinetobacter baumannii*. *PLoS Pathog* 2024;**20**:e1012529.
41. Jia Y, Wang Z, Zhu S, Wang Z, Liu Y. Disinfectants facilitate the transformation of exogenous antibiotic resistance genes *via* multiple pathways. *Ecotoxicol Environ Saf* 2023;**253**:114678.
42. Lin Z, Xu Z, Li Y, Wang Z, Chen T, Zhao X. Metabolic engineering of *Escherichia coli* for the production of riboflavin. *Microb Cell Fact* 2014;**13**:104.
43. Imlay JA. The molecular mechanisms and physiological consequences of oxidative stress: lessons from a model bacterium. *Nat Rev Microbiol* 2013;**11**:443−54.
44. Rush GF, Gorski JR, Ripple MG, Sowinski J, Bugelski P, Hewitt WR. Organic hydroperoxide-induced lipid peroxidation and cell death in isolated hepatocytes. *Toxicol Appl Pharmacol* 1985;**78**:473−83.
45. Bertani B, Ruiz N. Function and biogenesis of lipopolysaccharides. *EcoSal Plus* 2018;**8**:1−19.
46. Yang B, Tong Z, Shi J, Wang Z, Liu Y. Bacterial proton motive force as an unprecedented target to control antimicrobial resistance. *Med Res Rev* 2023;**43**:1068−90.
47. Tarin-Pello A, Suay-Garcia B, Perez-Gracia MT. Antibiotic resistant bacteria: current situation and treatment options to accelerate the development of a new antimicrobial arsenal. *Expert Rev Anti Infect Ther* 2022;**20**:1095−108.
48. Lafayette EA, de Almeida SMV, Cavalcanti Santos RV, de Oliveira JF, Amorim C, da Silva RMF, et al. Synthesis of novel indole derivatives as promising DNA-binding agents and evaluation of antitumor and antitopoisomerase I activities. *Eur J Med Chem* 2017;**136**:511−22.
49. Casu B, Arya T, Bessette B, Baron C. Fragment-based screening identifies novel targets for inhibitors of conjugative transfer of antimicrobial resistance by plasmid pKM101. *Sci Rep* 2017;**7**:14907.
50. Samosorn S, Bremner JB, Ball A, Lewis K. Synthesis of functionalized 2-aryl-5-nitro-1*H*-indoles and their activity as bacterial NorA efflux pump inhibitors. *Bioorg Med Chem* 2006;**14**:857−65.
51. Ambrus JI, Kelso MJ, Bremner JB, Ball AR, Casadei G, Lewis K. Structure−activity relationships of 2-aryl-1*H*-indole inhibitors of the NorA efflux pump in *Staphylococcus aureus*. *Bioorg Med Chem Lett* 2008;**18**:4294−7.
52. Adamczyk-Wozniak A, Sporzynski A. Merging electron deficient boronic centers with electron-withdrawing fluorine substituents results in unique properties of fluorinated phenylboronic compounds. *Molecules* 2022;**27**:3427.
53. Li G, Xia LJ, Zhou SY, Wang XR, Cui CY, He YZ, et al. Linoleic acid and α-linolenic acid inhibit conjugative transfer of an IncX4 plasmid carrying *mcr-1*. *J Appl Microbiol* 2021;**130**:1893−901.
54. Kok M, Bron G, Erni B, Mukhija S. Effect of enzyme I of the bacterial phosphoenolpyruvate: sugar phosphotransferase system (PTS) on virulence in a murine model. *Microbiology* 2003;**149**:2645−52.
55. Pickl A, Johnsen U, Schonheit P. Fructose degradation in the haloarchaeon *Haloferax volcanii* involves a bacterial type phosphoenolpyruvate-dependent phosphotransferase system, fructose-1-phosphate kinase, and class II fructose-1,6-bisphosphate aldolase. *J Bacteriol* 2012;**194**:3088−97.
56. Gassner M, Stehlik D, Schrecker O, Hengstenberg W, Maurer W, Rüterjans H. The phosphoenolpyruvate-dependent phosphotransferase system of *Staphylococcus aureus*. 2. 1H and 31P-nuclear-magnetic-resonance studies on the phosphocarrier protein HPr, phosphohistidines and phosphorylated HPr. *Eur J Biochem* 1977;**75**:287−96.
57. Alpert CA, Frank R, Stüber K, Deutscher J, Hengstenberg W. Phosphoenolpyruvate-dependent protein kinase enzyme I of *Streptococcus faecalis*: purification and properties of the enzyme and characterization of its active center. *Biochemistry* 1985;**24**:959−64.
58. Palmen R, Driessen AJ, Hellingwerf KJ. Bioenergetic aspects of the translocation of macromolecules across bacterial membranes. *Biochim Biophys Acta* 1994;**1183**:417−51.
59. Cascales E, Christie PJ. Agrobacterium VirB10, an ATP energy sensor required for type IV secretion. *Proc Natl Acad Sci U S A* 2004;**101**: 17228−33.
60. Min H, Seok YJ. Phosphotransferase system sugars immediately induce mutations of Cra in an *Escherichia coli* ptsH mutant. *Environ Microbiol* 2022;**24**:5425−36.
61. Hassan HM, Fridovich I. Intracellular production of superoxide radical and of hydrogen peroxide by redox active compounds. *Arch Biochem Biophys* 1979;**196**:385−95.

62. Shao M, Liu L, Liu B, Zheng H, Meng W, Liu Y, et al. Hormetic effect of pyroligneous acids on conjugative transfer of plasmid-mediated multi-antibiotic resistance genes within bacterial genus. *ACS Environ Au* 2022;**3**:105−20.
63. Guo Z, Feng S, Liang L, Wu Z, Min L, Wang R, et al. Assessment of the reversibility of resistance in the absence of antibiotics and its relationship with the resistance gene's fitness cost: a genetic study with *mcr-1*. *Lancet Microbe* 2024;**5**:100846.
64. Zhang M, Yang B, Shi J, Wang Z, Liu Y. Host defense peptides mitigate the spread of antibiotic resistance in physiologically relevant condition. *Antimicrob Agents Chemother* 2024;**68**:e0126123.
65. Li G, Ye Z, Zhang W, Chen N, Ye Y, Wang Y, et al. Rapid LC−MS/MS detection of different carbapenemase types in carbapenemase-producing Enterobacterales. *Eur J Clin Microbiol Infect Dis* 2022;**41**:815−25.
66. Han F, Zhang X, Chen Y, Zhao H, Wu J, Yu Y, et al. A simple allelic exchange method for efficient seamless knockout of up to 34-kbp-long gene cassettes in *Pseudomonas*. *Appl Biochem Biotechnol* 2023;**196**: 5616−30.
67. Baker CL, Seo KS, Park N, Rutter JK, Thornton JA, Pruett SB, et al. L-Arginine supplementation abrogates hypoxia-induced virulence of *Staphylococcus aureus* in a murine diabetic pressure wound model. *mSphere* 2024;**9**:e0077423.
68. Jiang M, Su YB, Ye JZ, Li H, Kuang SF, Wu JH, et al. Ampicillin-controlled glucose metabolism manipulates the transition from tolerance to resistance in bacteria. *Sci Adv* 2023;**9**. eade8582.
69. Krucinska J, Falcone E, Erlandsen H, Hazeen A, Lombardo MN, Estrada A, et al. Structural and functional studies of bacterial enolase, a potential target against Gram-negative pathogens. *Biochemistry* 2019;**58**:1188−97.
70. Cai J, Shi J, Chen C, He M, Wang Z, Liu Y. Structural−activity relationship-inspired the discovery of saturated fatty acids as novel colistin enhancers. *Adv Sci* 2023;**10**:e2302182.